

Banner appropriate to article type will appear here in typeset article

Prandtl number dependence of rotating internally heated convection

Rodolfo Ostilla-Mónico^{1†} and Ali Arslan²

¹Dpto. Ing. Mecánica y Diseño Industrial, Escuela Superior de Ingeniería, Universidad de Cádiz, Av. de la Universidad de Cádiz 10, 11519 Puerto Real, España

²Institute of Geophysics, ETH Zurich, 8092 Zurich, Switzerland

(Received xx; revised xx; accepted xx)

We investigate the influence of the Prandtl number (Pr) on penetrative internally heated convection (IHC) in both non-rotating and rotating regimes using three-dimensional direct numerical simulations. By varying Pr between 0.1 and 100, we show that the global mean temperature $\overline{\langle T \rangle}$ is not very sensitive to Pr , and is primarily controlled by the dynamics of the unstably stratified top boundary layer. In contrast, the Prandtl number dictates the behavior of the lower, stably stratified region and affects the vertical convective heat flux $\overline{\langle wT \rangle}$. In the non-rotating case, low Pr fluids exhibit a “symmetry recovery” where turbulent stirring agitates the stable layer, whereas high Pr fluids transition toward a “dead zone” of suppressed fluctuations. Under rotation, we find that $\overline{\langle wT \rangle}$ is enhanced across all Prandtl numbers, though global cooling efficiency, measured by the reduction in $\overline{\langle T \rangle}$, is only improved for $Pr \geq 1$ due to the emergence of Ekman pumping. These results demonstrate that while IHC shares some scaling similarities with Rayleigh-Bénard convection at the top boundary, the internal stratification creates a unique sensitivity to Pr that is critical for understanding heat transport in planetary and stellar interiors.

Key words: Turbulent convection, Rotating flows

1. Introduction

Turbulent convection is ubiquitous in nature. Driven by thermal or chemical gradients, this buoyancy-induced motion occurs throughout the atmospheres and interiors of rotating celestial bodies (Marshall & Schott 1999; Roberts & King 2013). In these systems, the competition between Coriolis-driven columnar structures and buoyant plumes dictates the mixing dynamics of atmospheres, mantles, and cores (Emanuel 1994; Aurnou *et al.* 2015). While the relative strength of these forces is traditionally characterized by the Rayleigh (R) and Ekman (E) numbers, a fundamental challenge in accurately modeling these environments lies in the extreme diversity of the fluid properties themselves. In particular, in Nature there is a vast range of Prandtl numbers (Pr), i.e. the ratio of viscous to thermal diffusion,

† Email address for correspondence: rodolfo.ostilla@uca.es

ranging from being $O(1)$ in atmospheres and 10^{-1} to 10^{-2} in liquid iron cores to $\sim 10^{23}$ in planetary mantles. Such variations fundamentally alter how heat is processed and how rotation constrains the flow.

The canonical model used to describe rotating convection is the Boussinesq approximation to the Navier-Stokes equations in a rotating frame, where the centrifugal force is neglected under either a constant density or small rotation assumptions (Ecke & Shishkina 2023). While the vast majority of literature focuses on convection driven by boundary temperature gradients in the classic Rayleigh-Bénard (RB) problem (Chandrasekhar 1953; Veronis 1959; Grossmann & Lohse 2000; Vorobieff & Ecke 2002; Stevens *et al.* 2013; Kunnen 2021; Ecke & Shishkina 2023; Lohse & Shishkina 2024), we instead focus on internally heated convection (IHC) between two perfectly conducting horizontal boundaries, where the fluid is heated volumetrically (Roberts 1967; Tritton & Zarraga 1967; Thirlby 1970; Kulacki & Goldstein 1972; Goluskin & Spiegel 2012; Goluskin & Van der Poel 2016). This configuration is fundamentally different from the classical Rayleigh-Bénard (RB) problem in several ways. Notably, IHC supports subcritical convection; the Rayleigh number determining the energy stability limit ($R_E \approx 26, 926.6$ for no-slip boundaries) is significantly lower than the Rayleigh number determining the linear instability threshold ($R_L \approx 37, 325.2$), whereas RB convection onsets via a pitchfork bifurcation at $R_E = R_L \approx 1, 707.76$ (Goluskin 2016; Chandrasekhar 1961). In addition, because heat is not transported from one boundary to the other, the standard Nusselt number used in RB studies (Lohse & Shishkina 2023) is not applicable. Instead, two global quantities are used to assess the effectiveness of convection: the mean temperature $\overline{\langle T \rangle}$, and the bottom heat flux heat fraction \mathcal{F}_B , where $\langle \cdot \rangle$ denotes averaging in the horizontal directions and time, and $\overline{\cdot}$ denote averages in the vertical direction.

In IHC, turbulence serves a dual role: it homogenizes the bulk temperature field while simultaneously creating an asymmetry in the heat flux leaving the boundaries, a flux that is perfectly balanced in the purely conductive state (Arslan *et al.* 2021). This asymmetry results in an unstably stratified thermal boundary layer at the top and a stably stratified layer at the bottom. The distinct structures of these layers contribute to scaling laws for viscous dissipation that remain less understood than their thermal counterparts (Wang *et al.* 2020; Arslan & Rojas 2025), with evidence suggesting that the viscous dissipation scales differently between two- and three-dimensional systems (Goluskin & Van der Poel 2016; Ostilla-Mónico & Arslan 2025).

The disparity between the top and bottom boundary layers is further accentuated by rotation. In rotating RB convection, the relative thicknesses of thermal and viscous boundary layers serve as a key diagnostic for identifying the transition from buoyancy-dominated flow to geostrophic turbulence (King *et al.* 2009; Maffei *et al.* 2021). A hallmark of this transition is the emergence and subsequent decoherence of Taylor columns as the rotation rate increases (Grooms *et al.* 2010; Kunnen *et al.* 2016). However, in rotating IHC, the stable bottom stratification interacts with the Ekman boundary layer, a phenomenon absent in boundary-driven systems which complicates the picture (Ostilla-Mónico & Arslan 2025). The effect of Pr on this phenomena is yet to be unveiled.

The morphology of these flows is also heavily dictated by the Prandtl number. In the limits of $Pr \rightarrow \infty$ and $Pr \rightarrow 0$, the momentum equation approaches forced Stokes and Euler flows, respectively. While Pr effects have been extensively documented for rotating RB convection (King & Aurnou 2013; Abbate & Aurnou 2023), the low- Pr regime is computationally demanding and remains relatively unexplored for IHC. One critical feature of rotating RB convection that vanishes at low Pr is the rotational enhancement of heat transport. In RB systems, this enhancement is attributed to Ekman pumping, which becomes ineffective at low Pr as high thermal diffusivity allows heat to escape the boundary layers

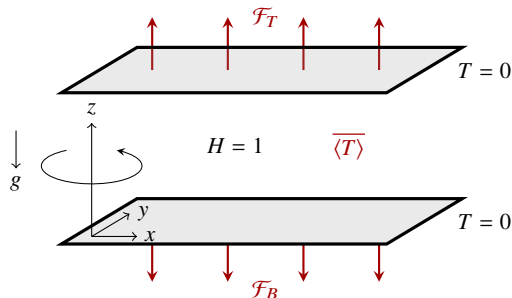


Figure 1: A non-dimensional schematic diagram for rotating uniform internally heated convection. The upper and lower plates are at the same temperature, and the domain is periodic in the x and y directions and rotates about the z axis. \mathcal{F}_B and \mathcal{F}_T are the mean heat fluxes out the bottom and top plates, $\overline{\langle T \rangle}$ the mean temperature, and g is the acceleration due to gravity.

before it can be vertically transported (Stevens *et al.* 2010a). Whether this suppression of transport enhancement persists in internally heated systems, where the driving is volumetric rather than boundary-based, remains an open question.

This manuscript builds upon the work of Ostilla-Mónico & Arslan (2025) to provide the first direct numerical simulations (DNS) of low- Pr through high- Pr rotating IHC. We conduct a parametric study across a wide range of R and E to quantify the bulk responses, horizontally averaged profiles, and boundary layer dynamics of this unique system. The paper is organised as follows. §2 describes the governing equations and simulation method. In §3, we present results for the variation of Pr on non-rotating IHC, while §4 contains results for the effect of Pr on rotating IHC. Finally, §5 briefly summarises the results obtained.

2. Setup

In this study, internally heated convection is examined within a fluid layer of depth d , bounded by two horizontal plates. We assume periodic boundary conditions in the horizontal dimensions with a domain aspect ratio of Γd . The physical properties of the fluid, i.e. the kinematic viscosity ν , the thermal diffusivity κ , the density ρ , the specific heat c_p and the thermal expansion coefficient α , are assumed constant. The system undergoes uniform internal heating at a rate H , and rotates at a constant angular velocity Ω about the vertical axis, with gravity g acting downward. We employ the Boussinesq approximation to account for density variations solely through the buoyancy term.

Following the scaling convention of Roberts (1967), the system is non-dimensionalised using d for length, d^2/κ for time, and $d^2H/(\kappa\rho c_p)$ for temperature. Under this non-dimensionalisation, the evolution of the velocity field, $\mathbf{u}(\mathbf{x}, t) = u(\mathbf{x}, t)\mathbf{e}_1 + v(\mathbf{x}, t)\mathbf{e}_2 + w(\mathbf{x}, t)\mathbf{e}_3$ and temperature field $T(\mathbf{x}, t)$ is governed by the following equations:

$$\nabla \cdot \mathbf{u} = 0, \quad (2.1)$$

$$\partial_t \mathbf{u} + \mathbf{u} \cdot \nabla \mathbf{u} + E^{-1} \mathbf{e}_3 \times \mathbf{u} = -\nabla p + Pr \nabla^2 \mathbf{u} + Pr R T \mathbf{e}_3, \quad (2.2)$$

$$\partial_t T + \mathbf{u} \cdot \nabla T = \nabla^2 T + 1, \quad (2.3)$$

the velocity and temperature fields are constrained by no-slip ($\mathbf{u} = 0$) and isothermal ($T = 0$) conditions at both the upper and lower boundaries.

The dynamical response of the system is determined by three fundamental dimensionless groups: the Rayleigh number (R), the Ekman number (E), and the Prandtl number (Pr):

$$R = \frac{g\alpha Hd^5}{\rho c_p \nu k^2}, \quad E = \frac{\nu}{2\Omega d^2}, \quad Pr = \frac{\nu}{k}. \quad (2.4)$$

Additionally, we can obtain the convective Rossby number, $Ro = E\sqrt{R/Pr}$, to quantify the competition between buoyant and Coriolis forces.

The governing equations 2.1-2.3 are numerically integrated using AFiD (Van Der Poel *et al.* 2015). This open-source code employs a second-order centered finite difference scheme and has been thoroughly benchmarked for internal heating scenarios (Goluskin & Van der Poel 2016; Kazemi *et al.* 2022; Ostilla-Mónico & Arslan 2025).

In this study, we extend the results of Ostilla-Mónico & Arslan (2025) by varying the Prandtl number to explore the (Pr, R, E) parameter space of rotationally-affected convection. We vary Pr in the range $Pr \in [0.1, 10]$, R in the range $R \in [3.16 \times 10^5, 10^{10}]$ and $E \in [10^{-6}, \infty]$. To be more specific, we extend the parameter space explored in Ostilla-Mónico & Arslan (2025) by repeating the (R, E) pairs for four different values of Pr : $Pr = 0.1, 0.3, 3$ and 10 . We also run a series of non-rotating cases ($E = \infty$) cases for $Pr = 30$ and 100 .

The non-dimensional periodicity length Γ is selected following the values of Ostilla-Mónico & Arslan (2025) for the $Pr = 1$ cases, except for $R = 10^9$ where Γ is reduced to 1. For $Pr \geq 1$, this ensures that $\overline{\langle T \rangle}$ and $\overline{\langle wT \rangle}$ remain independent of domain size. For $Pr \leq 1$, a dependence $\overline{\langle wT \rangle}$ on the horizontal periodicity length Γ is introduced. While this does not change the overall physics of the problem, we quantify its effect in Appendix A.

The resolution adequacy is measured by the exact relationships:

$$\overline{\langle \epsilon_v \rangle} \equiv \overline{\langle |\nabla^2 \mathbf{u}| \rangle} = R \overline{\langle wT \rangle}, \quad (2.5)$$

$$\overline{\langle \epsilon_\theta \rangle} \equiv \overline{\langle |\nabla^2 T| \rangle} = \overline{\langle T \rangle}. \quad (2.6)$$

To guarantee numerical accuracy, we ensure that both sides of the equation do not deviate by more than 1%. This criterion provides a more stringent resolution constraint than those based solely on the mean Kolmogorov or Batchelor scales, yet it is recognized as sufficient for characterizing thermal convection (Stevens *et al.* 2010b).

We use the resolutions of Ostilla-Mónico & Arslan (2025), which satisfy the criteria above for all Pr . In the most adverse cases, the discretisation used in this manuscript has a maximum point distance of 1.5 Kolmogorov length-scales. In the non-rotating case, the upper thermal boundary layer, whose extent can be estimated by $\overline{\langle T \rangle} / (\frac{1}{2} + \overline{\langle wT \rangle})$ is resolved by at least six points. As rotation increases, the number of points in the z direction must be increased to resolve the increasingly thinner Ekman (velocity) boundary layers.

For $Pr = 0.3$ and $Pr = 3$, simulations are initialised from initial conditions at $Pr = 1$ with the same (R, E) parameter values, while for $Pr = 0.1$ and $Pr = 10$ they are started from the $Pr = 0.3$ and $Pr = 3$ cases respectively. After transients, statistics are collected for a time interval of length t_{av} which ensure that the time-averaged values of $\overline{\langle T \rangle}$ and $\overline{\langle wT \rangle}$ are less than 1% different from those corresponding to half the run-time. In general t_{av} depends on both Pr and R , as the flow becomes faster with increasing R (decreasing the necessary averaging time) but increases with Pr as the flow becomes slower.

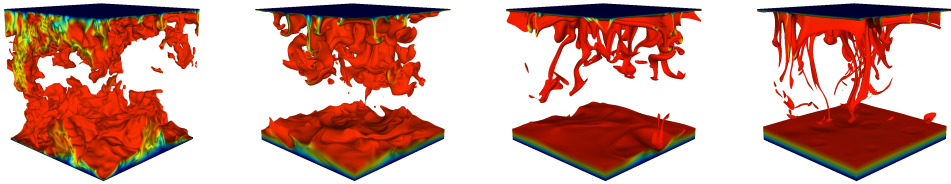


Figure 2: Volumetric visualisation of the instantaneous temperature field without rotation for $R = 10^{10}$ and from left to right: $Pr = 0.1$, $Pr = 1$, $Pr = 10$ and $Pr = 100$.

3. Non-rotating IHC

3.1. Flow visualization

We begin by examining cases without rotation to characterise the influence of the Prandtl number on the flow structure. Figure 2 illustrates the morphological evolution of the flow as Pr is varied. In all instances, convective structures and plumes originate within the unstably stratified upper boundary layer before descending into the bulk. At lower Prandtl numbers ($Pr = 0.1$ and $Pr = 1$), these structures vigorously stir the lower boundary layer, generating widespread turbulence throughout the domain. Conversely, for $Pr = 10$, the dynamics of the bottom boundary layer are noticeably diminished, and the flow field is dominated by coherent, elongated plume-like structures. For $Pr = 100$, the plume structures become even thinner, while the bottom of the domain is practically quiescent.

3.2. Global quantities

To characterise the global system response, we consider three primary dimensionless parameters: the bottom heat flux fraction \mathcal{F}_B , the volume-averaged temperature $\overline{\langle T \rangle}$ and the wind Reynolds number $Re_w = U_w d / \nu$. Here, the characteristic wind velocity U_w is defined as the root-mean-square velocity:

$$U_w = \overline{\langle u^2 + v^2 + w^2 \rangle}^{1/2}. \quad (3.1)$$

The top panels of Figure 3 depict the behaviour of \mathcal{F}_B across the (R, Pr) parameter space. We note that \mathcal{F}_B is the quantity conventionally used when representing mathematical upper bounds, but one could also represent \mathcal{F}_T , the upper heat fraction, or the vertical convection $\overline{\langle wT \rangle}$. As in the statistically stationary state of internally heated convection, the total heat generated must be balanced by the flux through the boundaries, the three quantities are not independent but instead related through the relationships:

$$\mathcal{F}_B + \mathcal{F}_T = 1, \quad \mathcal{F}_B = \frac{1}{2} - \overline{\langle wT \rangle}, \quad \mathcal{F}_T = \frac{1}{2} + \overline{\langle wT \rangle}.$$

Therefore, representing $\overline{\langle wT \rangle}$ is equivalent to representing \mathcal{F}_B (or \mathcal{F}_T). In general, $\overline{\langle wT \rangle} \geq 0$, due to the asymmetry introduced by convection. Consequently, \mathcal{F}_B can be seen as a proxy for the convective heat transport efficiency, but its behaviour is independent from that of $\overline{\langle T \rangle}$.

Across the investigated parameter space, \mathcal{F}_B exhibits a consistent trend regardless of Pr : it decreases as R increases, indicating that a larger proportion of heat escapes through the top boundary. This trend is consistent with enhanced vertical heat transport at higher thermal driving. While 2-D simulations have previously reported non-monotonic behaviour ($Pr \geq 1$) or weak R -dependence ($Pr < 1$) due to flow organisation affected by geometric constraints (Goluskin & Van der Poel 2016), our 3-D results show that \mathcal{F}_B decreases monotonically with

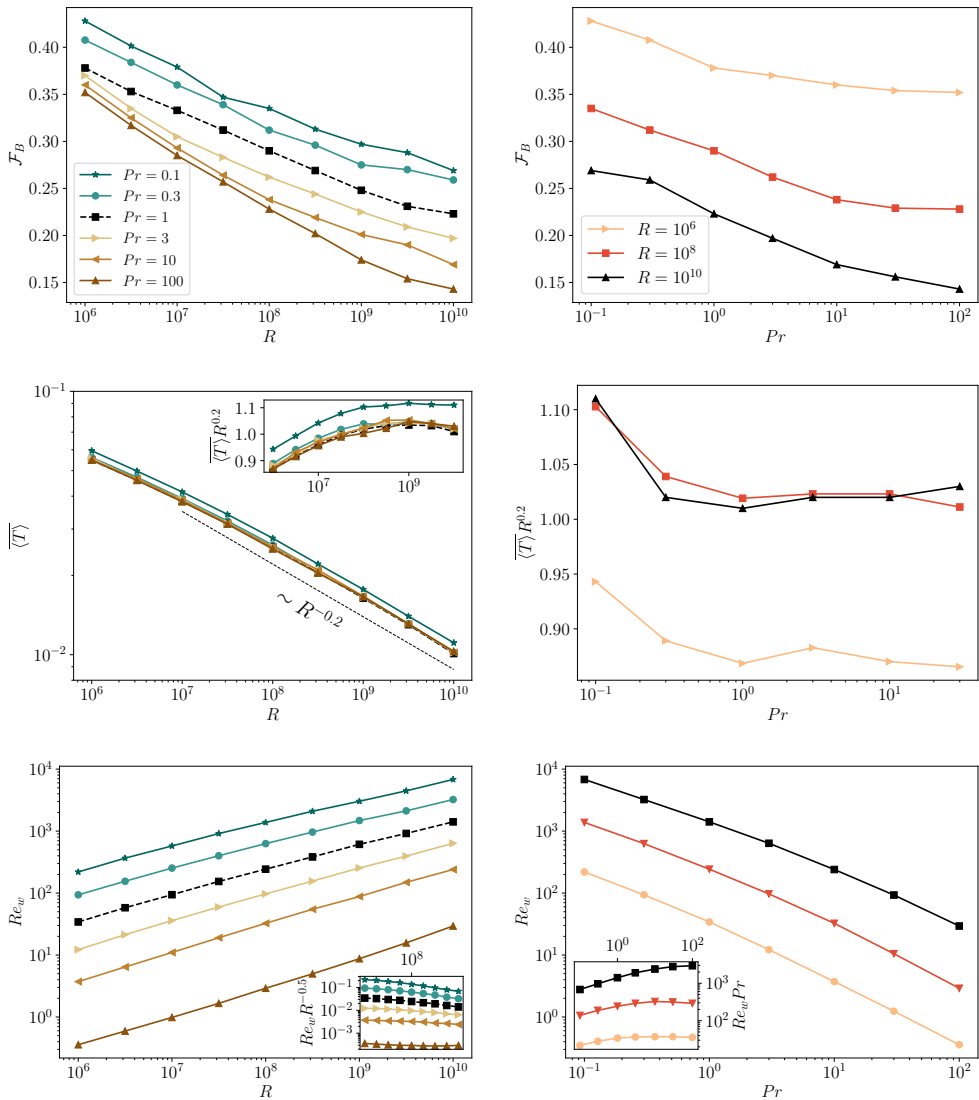


Figure 3: Global responses. \mathcal{F}_B (top), $\overline{\langle T \rangle}$, (middle) and Re_w (bottom) against R (left) and Pr (right). For clarity, only selected values of Pr are shown on the left column plots.

R when such constraints are removed. Furthermore, the 3-D configuration yields significantly higher vertical convective heat transfer, and thus lower \mathcal{F}_B values, across all reported Prandtl numbers.

In general the Pr dependence is such that smaller Pr generally results in less efficient heat transport vertically. While the visualisations in Figure 2 suggest a more turbulent bottom boundary layer at low Pr , the high thermal diffusivity at these values renders vertical convection less efficient. In contrast, at high Pr , the flow produces intense plumes that transport heat more effectively despite weaker overall stirring. Notably, the Pr dependence becomes weaker but remains unsaturated even at $Pr = 100$.

The middle panels of Figure 3 show the volume-averaged temperature $\overline{\langle T \rangle}$, which follows a

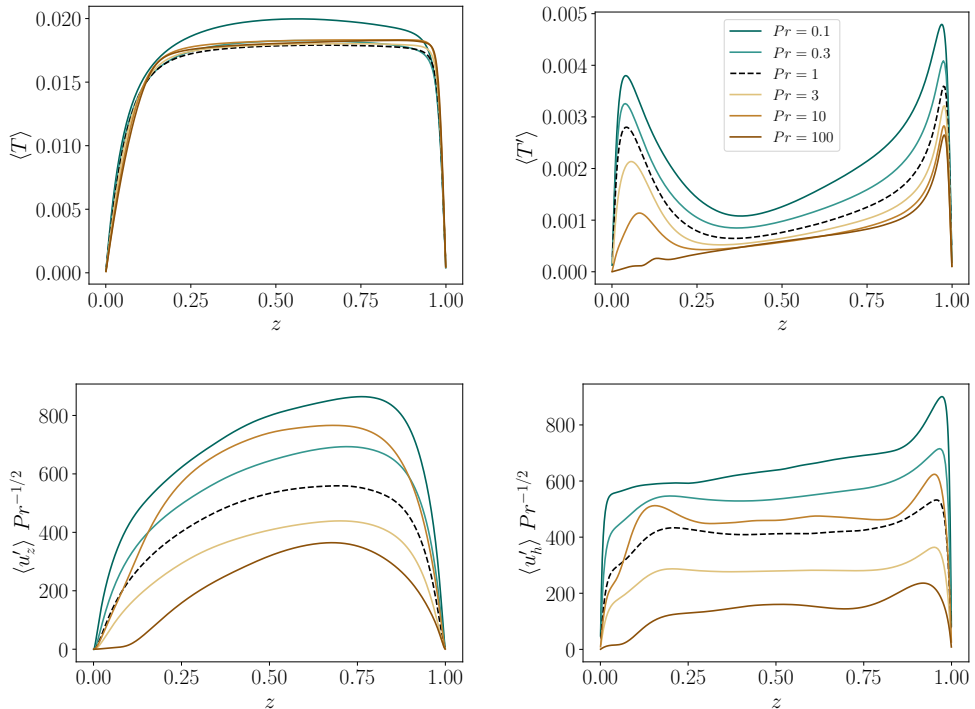


Figure 4: Plots of the horizontally averaged temperature and temperature fluctuation against z (top), and scaled horizontally averaged vertical velocity and horizontal velocity fluctuations against z (bottom). All plots are for $R = 10^9$ and varying Prandtl numbers.

decreasing trend with R . We find an approximate scaling of $\overline{\langle T \rangle} \sim R^{-0.2}$ across all simulated Pr . This scaling, previously noted for $Pr = 1$ by [Goluskin & Van der Poel \(2016\)](#), relates to the dominance of thermal dissipation within the top boundary layer ([Ostilla-Mónico & Arslan 2025](#)). The influence of Pr on the mean temperature is minimal, showing significant variation only at $Pr = 0.1$, a behaviour reminiscent of the behaviour of the Nusselt number observed in standard Rayleigh-Bénard convection of which $\overline{\langle T \rangle}$ is a direct analog in this system.

Finally, the bottom panels of Figure 3 show the wind Reynolds number Re_w . As expected, Re_w increases with R and decreases with Pr due to higher viscous dissipation. Power-law fits of the form $Re_w \sim R^\alpha$ yield exponents in the range $0.38 < \alpha < 0.5$, with α increasing alongside Pr . For the highest Pr values, we observe a rough scaling of $Re_w \sim Pr^{-1}$. This suggests that at low Re_w , where the flow is nonlinear but not yet fully turbulent, the system effectively mimics infinite- Pr behavior. However, as R increases and hydrodynamic turbulence becomes significant, this scaling law eventually breaks down.

3.3. Temperature and velocity statistics

To gain further insight into the global behaviors observed, we examine the local statistics of the fluid fields. The top two panels of Figure 4 display the mean temperature $\langle T \rangle$ and RMS fluctuations $\langle T' \rangle = \sqrt{\langle T^2 \rangle - \langle T \rangle^2}$ profiles for various Pr at $R = 10^9$. The mean temperature profiles are largely insensitive to the Prandtl number, with the exception of the low- Pr regime, where slightly higher values are observed. Despite these minor magnitude

differences, the profile morphology remains consistent with two distinct, steep boundary layers and a relatively flat bulk region.

Substantial differences emerge, however, when comparing the temperature fluctuations $\langle T' \rangle$. Fluctuations are notably higher at small Pr , and the asymmetry between the top and bottom boundary layers intensifies as Pr increases. This aligns with our qualitative visualisations. At low Pr , vigorous stirring occurs within the stably stratified bottom boundary layer, even though this ultimately corresponds to lower net heat transport. For the highest Pr cases, fluctuations near the bottom plate vanish entirely as the stable stratification and high viscosity effectively damp turbulence, restricting flow activity to the bulk and the upper boundary.

Turning to the velocity statistics, the bottom panels of Figure 4 show the profiles for horizontal velocity fluctuations $\langle u'_h \rangle = \langle u_x'^2 + u_y'^2 \rangle^{1/2}$ and vertical fluctuations $\langle u'_z \rangle$. Note that we have scaled these profiles by $Pr^{-1/2}$ to compensate for the diffusive time-scale used in the non-dimensionalisation. This compensation allows for a more direct comparison of the profile shapes. Without this compensation, the $Pr = 100$ magnitudes would dwarf the others, obscuring qualitative shifts.

The vertical fluctuations generally exhibit a profile that is relatively independent of Pr , with a gradual increase from the bottom wall (which is steeper at low Pr), followed by a sharp drop to zero at the top boundary. Consistent with the temperature statistics, for $Pr = 100$, a stagnant zone is evident at the bottom plate where fluid motion is entirely suppressed.

The horizontal velocity fluctuations reveal a more intricate structure. While all cases exhibit a flat bulk region and a prominent peak representing the velocity boundary layer near the top, the bottom stable layer demonstrates complex Pr -dependence. At $Pr = 0.1$, there is a simple monotonic increase to the bulk level. However, at $Pr = 0.3$, two distinct regions emerge within the bottom layer, an initial sharp rise followed by a more gradual increase. This bifurcation becomes more pronounced with increasing Prandtl. As suggested by [Ostilla-Mónico & Arslan \(2025\)](#), these transitions mark the distinction between the viscous boundary layer and the deeper-extending stably stratified region. At higher Prandtl number, the velocity boundary layer is completely damped as the stably stratified zone of is stagnant.

Figure 5 compares the thermal and (top) velocity boundary layer thicknesses. The thickness of the top thermal boundary layer remains nearly constant across the Prandtl number range explored, which is consistent with the nearly constant mean temperature $\langle T \rangle$ (analogous to the behavior of a Nusselt number). Conversely, the bottom thermal boundary layer thickens with increasing Pr , except at $Pr = 100$ where the lack of a distinct temperature fluctuation peak makes identification difficult. Finally, the top velocity boundary layer thickens as Pr increases, a direct consequence of the increased kinematic viscosity.

3.4. Dissipation rates

To conclude the analysis of non-rotating IHC, we examine the local thermal $\langle \overline{\epsilon_\theta} \rangle$ and viscous $\langle \overline{\epsilon_\nu} \rangle$ dissipation rates. These quantities are coupled to the global parameters $\langle wT \rangle$ and $\langle T \rangle$ via the exact relations in Eqs. 2.5–2.6. Identifying the relative contributions of the bulk and boundary layers to these dissipation rates is a standard approach in thermal convection studies for determining the factors that limit global transport ([Grossmann & Lohse 2000](#); [Wang et al. 2020](#)).

The top-left panel of Figure 6 shows the local thermal dissipation $\langle \overline{\epsilon_\theta} \rangle$. Remarkably, the profile of $\langle \overline{\epsilon_\theta} \rangle$ is largely independent of Pr . While dissipation is slightly elevated at the bottom plate for low Pr , the statistics are overwhelmingly dominated by the top plate. This is confirmed in the top-right panel. For all cases, the top boundary layer accounts for more than

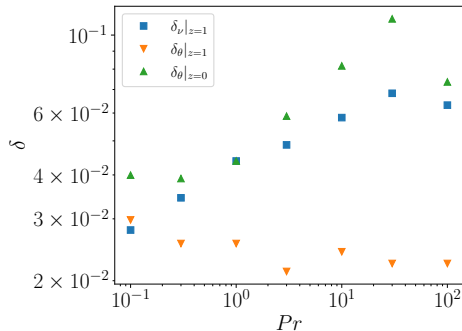


Figure 5: Thermal and viscous boundary layer sizes for $R = 10^9$ and all values of Pr simulated.

half of the total thermal dissipation. As in [Ostilla-Mónico & Arslan \(2025\)](#), the top-layer thermal dissipation scales with driving as $R^{-0.2}$, which directly underpins the global scaling $\overline{\langle T \rangle} \sim R^{-0.2}$.

In contrast, the viscous dissipation $\overline{\langle \epsilon_v \rangle}$ (bottom-left panel) shows large sensitivity to Pr . Viscous dissipation is significant at the bottom plate only for small Pr , and even then, it remains comparable to bulk levels. At high Pr , dissipation at the bottom boundary drops to near zero due to the suppression of velocity fluctuations. Meanwhile, dissipation in the top half of the domain increases, reflecting the enhanced convective efficiency $\overline{\langle wT \rangle}$ at higher Pr .

Following the methodology of [Ostilla-Mónico & Arslan \(2025\)](#), we decompose these contributions into contributions from top and bottom boundary layers, as well as bulk for $\overline{\langle \epsilon_\theta \rangle}$, and top boundary layer and a combined “bulk and bottom” region for $\overline{\langle \epsilon_v \rangle}$. The results in the bottom-right panel of Figure 6 confirm that for all Pr , the total viscous dissipation is dominated by the bulk. This reinforces the finding that 3-D IHC flows are bulk-dominated, contrasting with the boundary-layer-dominated results reported for 2-D simulations ([Wang et al. 2020](#)). This can also be related to the relatively smaller values of \mathcal{F}_B (larger values of $\overline{\langle wT \rangle}$) seen for high Pr . The dissipation in the bulk is stronger at high Pr , and as $\overline{\langle \epsilon_v \rangle}$ is dominated by the bulk, this results in a larger $\overline{\langle wT \rangle}$.

3.5. Summary

In conclusion, our analysis of the Pr -dependence in non-rotating IHC reveals that Prandtl number variations primarily influence the behaviour of the stably stratified lower layer. At low Pr , this region is vigorously agitated by the system’s turbulence, which effectively “recovers” some of the top-down symmetry otherwise broken by the stable stratification. Conversely, at high Pr , the dynamics are dominated by plumes and concentrated within the upper regions of the domain. For the highest Pr value investigated, the stable stratification renders the fluid near the bottom plate completely quiescent, resulting in a “dead zone”.

Remarkably, these profound shifts in flow morphology and local statistics are not significantly reflected in the volume-averaged temperature, $\overline{\langle T \rangle}$. This stability is due to the mean temperature being primarily governed by the upper thermal boundary layer—a region that remains largely insensitive to Pr . However, the vertical convective heat flux $\overline{\langle wT \rangle}$ (and by extension, the heat fraction \mathcal{F}_B) does exhibit a Pr -dependence; at low Pr , more heat is evacuated through the lower boundary as a result of the turbulence-driven symmetry recovery.

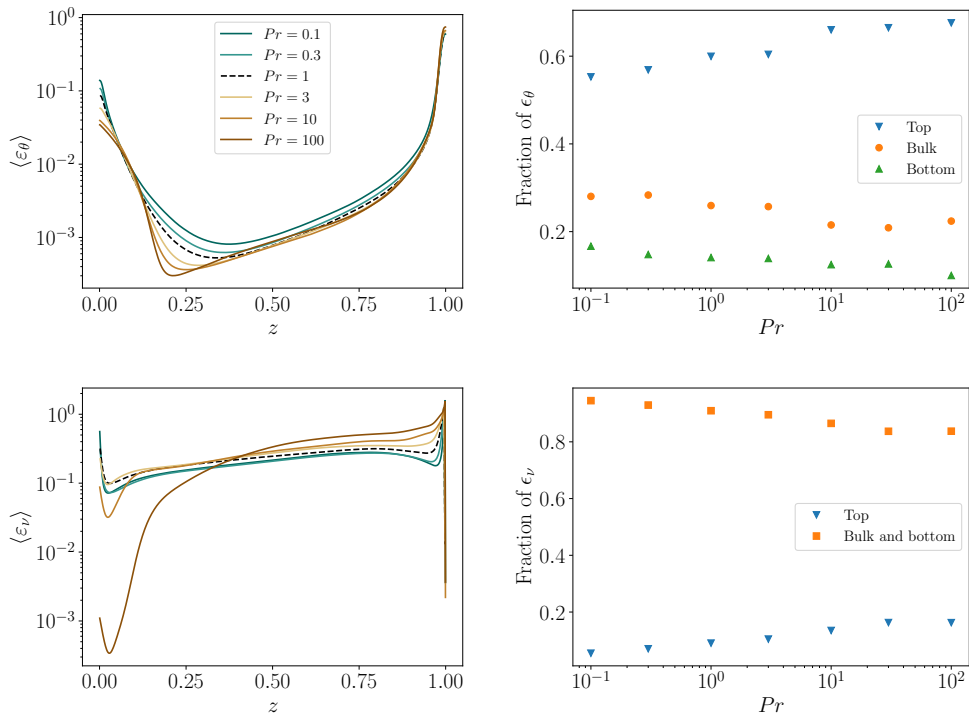


Figure 6: Left column: horizontally averaged thermal and viscous energy dissipation rate profiles for $R = 10^9$ and varying Pr . Right column: Relative contributions to the dissipation rates of the flow regions as a function of Pr .

4. Rotationally-affected IHC

Following our characterisation of the non-rotating system, we now examine how the Prandtl number influences IHC in the presence of rotation, extending the parameter space explored by [Ostilla-Mónico & Arslan \(2025\)](#). The introduction of the Coriolis force fundamentally alters the transport mechanisms and flow morphology, often competing with the Pr number effects discussed in the previous section.

4.1. Flow visualisation

We begin by assessing the impact of rotation on the global flow topology. Figure 7 displays volumetric visualisations of the instantaneous temperature field at a constant Ekman number $E = 10^{-4}$ for three representative Prandtl numbers. Consistent with observations in classic rotating Rayleigh-Bénard convection (RRBC), the degree to which rotation reorganises the flow is highly sensitive to Pr .

At $Pr = 0.1$, the flow remains largely unaffected by rotation, it maintains a highly turbulent state characterised by significant fluctuation within the lower boundary layer, similar to the non-rotating case. In contrast, at $Pr = 1$, the influence of rotation becomes apparent as the flow begins to organise into coherent structures, with plumes clustering in localised regions of the domain. The most dramatic shift occurs at $Pr = 10$, where the convective structures are transformed into elongated, vertically aligned columns. This morphological transition is a hallmark of rotationally constrained flow ([Zhong *et al.* 2009](#); [Kunnen 2021](#)), and is driven by Ekman pumping mechanisms that enhance vertical transport within the columnar cores.

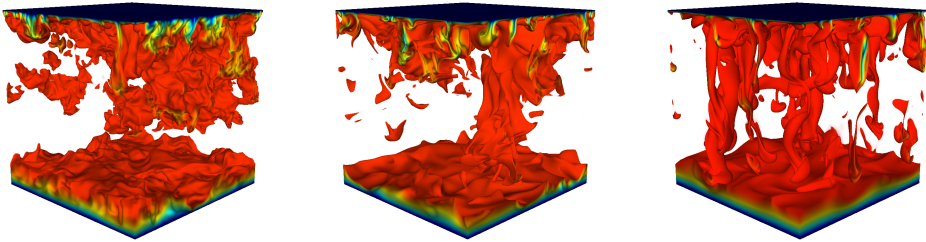


Figure 7: Volumetric visualisation of the instantaneous temperature field for $R = 10^{10}$, $E = 10^{-4}$. From left to right: $Pr = 0.1$, $Pr = 1$ and $Pr = 10$.

4.2. Global Quantities

To evaluate the influence of rotation on the global system response, Figure 8 presents the vertical convective flux $\overline{\langle wT \rangle}$, the mean temperature $\overline{\langle T \rangle}$, and the wind Reynolds number Re_w , all normalised by their respective non-rotating values (denoted by the subscript ∞). These quantities are plotted against both the Ekman number E and the inverse Rossby number $1/Ro$ at a fixed Rayleigh number $R = 10^9$.

When it comes to vertical convection, $\overline{\langle wT \rangle}$, rotation enhances this magnitude across all investigated Prandtl numbers. For lower Pr , we observe an increase of up to 30% at intermediate rotation rates ($0.1 \leq 1/Ro \leq 1$), whereas for $Pr = 10$, this enhancement is more modest, peaking at approximately 10%. As discussed in Appendix A, while the specific magnitude of the increase at $Pr = 0.1$ depends on the domain aspect ratio Γ , the qualitative trend—characterised by an initial rise in $\overline{\langle wT \rangle}$ followed by a subsequent decline at very high rotation rates—remains robust across different horizontal periodic lengths.

The physical origin of this convective enhancement is not immediately evident from global metrics alone. The middle column of Figure 8 shows that the wind Reynolds number Re_w decreases monotonically with rotation for all Pr . This suggests that Re_w does not capture the fundamental shifts in flow topology, however, it does indicate that the rise in $\overline{\langle wT \rangle}$ is not a by product of increased overall turbulence, but rather a reorganisation of the transport mechanism itself.

Before further discussing $\overline{\langle wT \rangle}$, we turn to the inverse mean temperature $\overline{\langle T \rangle}_\infty / \overline{\langle T \rangle}$ (a proxy for heat transfer efficiency). This quantity shows significant enhancement only for $Pr \geq 1$. As previously noted, the behavior of this quantity in IHC is analogous to the Nusselt number in rotating Rayleigh-Bénard convection (RRBC). Consistent with RRBC literature, increased convective efficiency is primarily restricted to higher Prandtl numbers where Ekman pumping plays a dominant role (Kunnen 2021; Ecke & Shishkina 2023). At low Pr , no such optimum is observed, and the efficiency gain is absent.

The behaviour of $\overline{\langle wT \rangle}$ and $\overline{\langle T \rangle}$ becomes more evident at low Pr when rotation is present. Total heat transport is essentially limited by the top thermal boundary layer (c.f. §3.4), while $\overline{\langle wT \rangle}$ is linked to the asymmetry between top and bottom boundary layers. An increase of rotation leads to two phenomena that increase the asymmetry of heat transport. At low Pr , higher thermal diffusion maintains the stably stratified region at the bottom, increasing the asymmetry between top and bottom, increasing the vertical heat transport. At high Pr , rotation enhances heat transport at the top boundary layer through Ekman pumping, increasing both plate asymmetry. For $\overline{\langle T \rangle}$, at low Pr , increased diffusion inhibits the effect of transport by columnar flows and rotation does not enhance the turbulent mixing. The

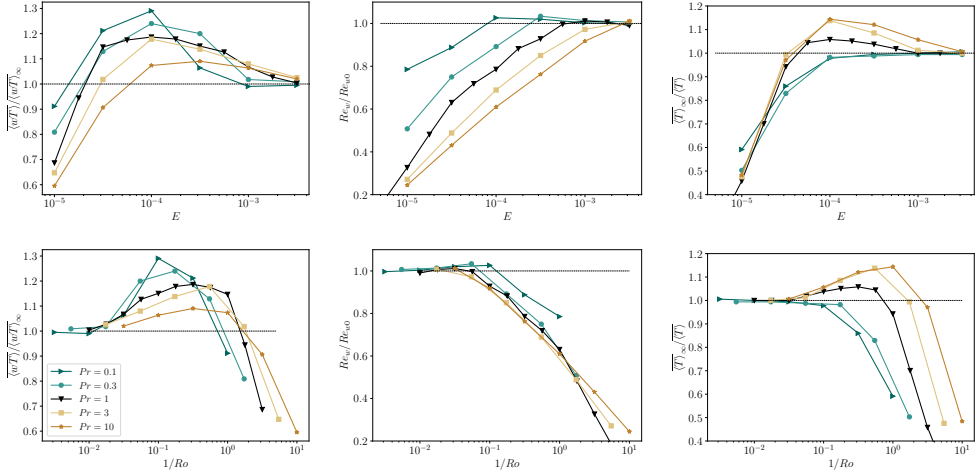


Figure 8: Changes in the global responses with rotation for $R = 10^9$. $\overline{\langle wT \rangle} / \overline{\langle wT \rangle}_\infty$ (left column), $Re_w / Re_{w,\infty}$ (middle column) and $\overline{\langle T \rangle}_\infty / \overline{\langle T \rangle}$ (right column) against E (top row) and $1/Ro$ (bottom row).

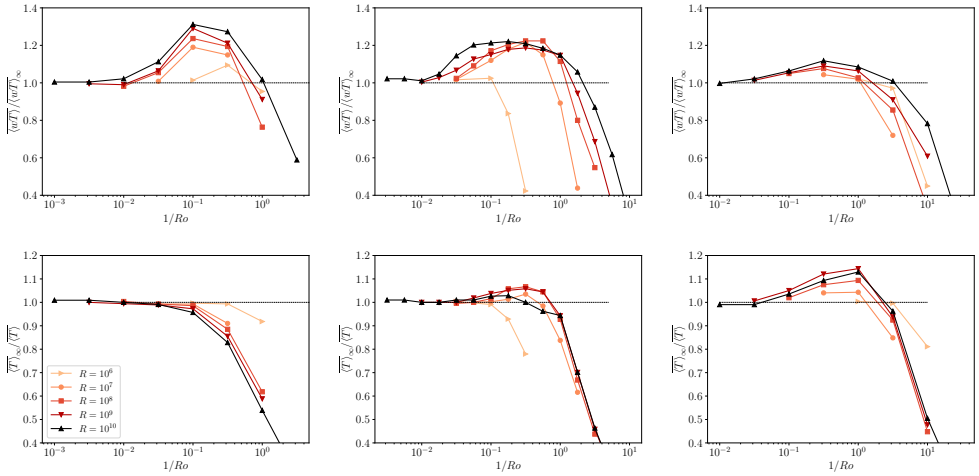


Figure 9: Changes in the global responses $\overline{\langle wT \rangle}$ and $\overline{\langle T \rangle}$ with rotation for $Pr = 0.1$ (left column), $Pr = 1$ (middle column) and $Pr = 10$ (right column).

opposite occurs at high Pr , where Ekman pumping is effective at enhancing mixing and thereby increasing $\overline{\langle T \rangle}$ for intermediate values of E .

Figure 9 further illustrates the rotational dependence of $\overline{\langle wT \rangle}$ and $\overline{\langle T \rangle}$ across a range of Rayleigh numbers for $Pr = 0.1, 1$, and 10 . Here, the analogy between $\overline{\langle T \rangle}$ and Nusselt number in RRBC becomes particularly apparent, not only is the effect limited to $Pr \geq 1$, but the decrease in $\overline{\langle T \rangle}$ is confined to a specific range of R . For instance, at $Pr = 1$, the effect begins to diminish at the highest Rayleigh numbers. In contrast, the enhancement of $\overline{\langle wT \rangle}$ persists across the entire parameter space and is notably more pronounced at lower Pr . These divergent trends underscore that the mechanisms driving vertical convective transport are physically distinct from those governing global heat transport efficiency.

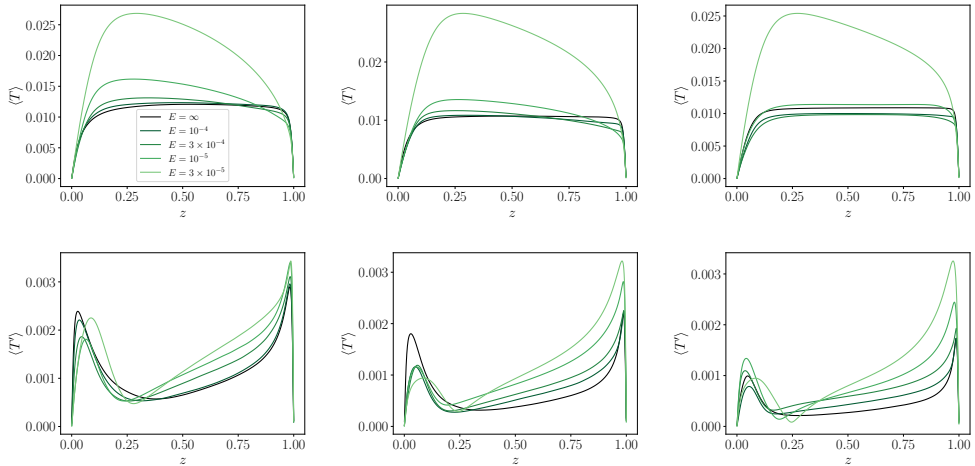


Figure 10: Mean $\langle T \rangle$ (top row) and fluctuation $\langle T' \rangle$ (bottom row) profiles for $R = 10^{10}$ for several values of E and $Pr = 0.1$ (left column), $Pr = 1$ (middle) and $Pr = 10$ (right column).

4.3. Temperature and velocity statistics

We now examine the influence of rotation on local statistics. Figure 10 illustrates the mean temperature and fluctuation profiles for $R = 10^{10}$ across various Pr and E values. Consistent with non-rotating IHC, the Prandtl number does not fundamentally alter the morphology of the mean temperature profiles. However, the introduction of rotation induces a notable bulk temperature gradient. The profiles transition from a relatively flat central region to a distinct slope as $1/Ro$ increases. This phenomenon is quantified in the left panel of Figure 11, which demonstrates that the gradient emerges once Coriolis forces become significant relative to convective forces ($1/Ro \geq 1$). While the onset of this gradient shows a slight Pr dependence, the inverse Rossby number remains the most robust parameter for collapsing this behavior, as it accounts for the R -dependence more effectively than the Ekman number (Ostilla-Mónico & Arslan 2025).

The temperature fluctuations $\langle T' \rangle$ exhibit a more nuanced Pr dependence. In general, rotation enhances fluctuations throughout the domain, except near the lower boundary. At $E = 3 \times 10^{-5}$, fluctuations across different Pr values become comparable, contrasting with the non-rotating case where low Pr significantly dominated. In the bottom boundary layer, rotation suppresses fluctuations for $Pr = 0.1$ and $Pr = 1$. Interestingly, for $Pr = 10$, fluctuations initially decrease before rising again at high rotation rates, likely reflecting a reorganisation of the flow topology that more vigorously agitates the lower stable region.

Regarding boundary layer thickness (Figure 11, right), the top thermal boundary layer remains largely independent of Pr and constant in size until $1/Ro \approx 1$, where it begins to thicken. The bottom thermal boundary layer shows greater variation without a singular trend, though it generally increases in size once rotation becomes dominant.

Velocity statistics (Figure 12) reveal that vertical fluctuations $\langle u'_z \rangle$ are largely independent of Pr , though higher Pr leads to stronger suppression at comparable E . The presence of regions near the bottom plate where the overall value of fluctuations is small is more apparent at high Pr , as the stably stratified layer is even less active in these cases.

Horizontal fluctuations $\langle u'_h \rangle$ display a richer phenomenology. At small Pr , rotation initially stabilises the bottom region before the formation of an Ekman boundary layer triggers a

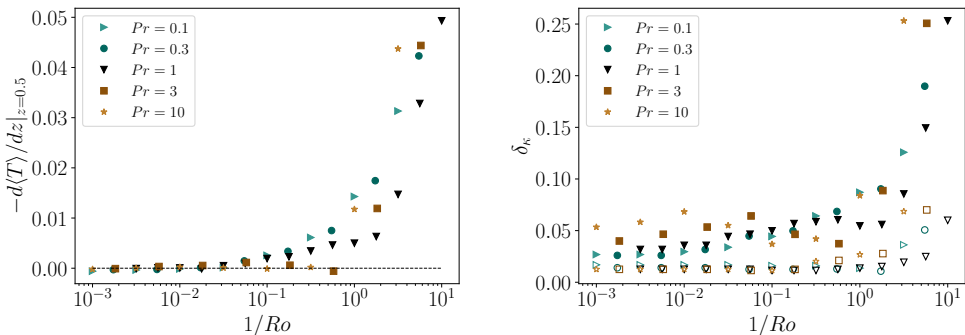


Figure 11: Left: temperature gradient in the bulk as a function of rotation for $R = 10^{10}$. Right: top (hollow symbols) and bottom (solid symbols) thermal boundary layer size as a function of rotation for $R = 10^{10}$ and several values of Pr .

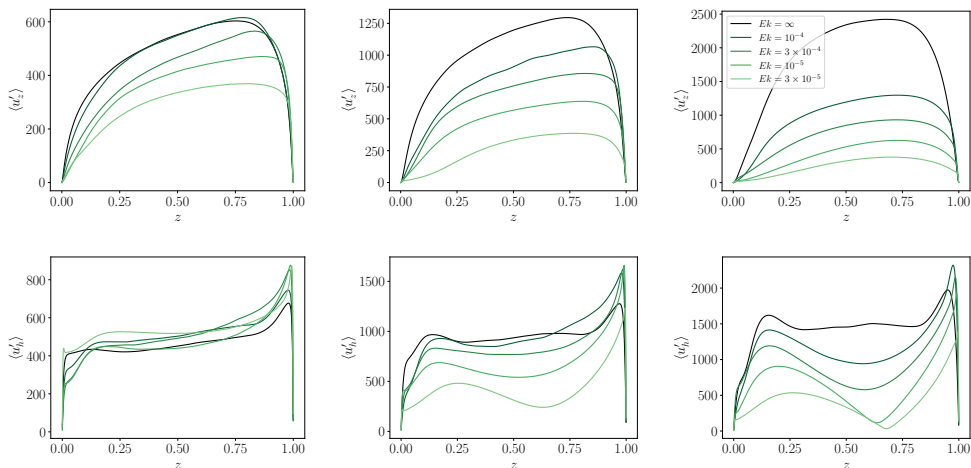


Figure 12: Vertical $\langle u'_z \rangle$ (top row) and horizontal $\langle u'_h \rangle$ (bottom row) velocity fluctuation profiles for $R = 10^{10}$ for several values of E and $Pr = 0.1$ (left column), $Pr = 1$ (middle) and $Pr = 10$ (right column).

secondary increase in fluctuations at very small E . For $Pr = 1$ and $Pr = 10$, this stabilisation is even more pronounced, with the bulk and lower regions becoming significantly damped before the eventual appearance of the Ekman layer, marked as a new peak close to the bottom plate, once E is small enough.

At the top plate, the velocity boundary layer thickness scales as $\delta_{\nu}|_{z=1} \sim E^{1/2}$ (Figure 13, left), confirming the appearance of Ekman layers across all Pr . In addition, the ratio of thermal to velocity boundary layer thickness (right panel) shows a crossover at $E \sim 10^{-4}$ across all Pr . As discussed in [Ostilla-Mónico & Arslan \(2025\)](#) for $Pr = 1$, this diagnostic, proposed for the geostrophic transition in RRBC, does not identify this crossover in IHC regardless of the Prandtl number.

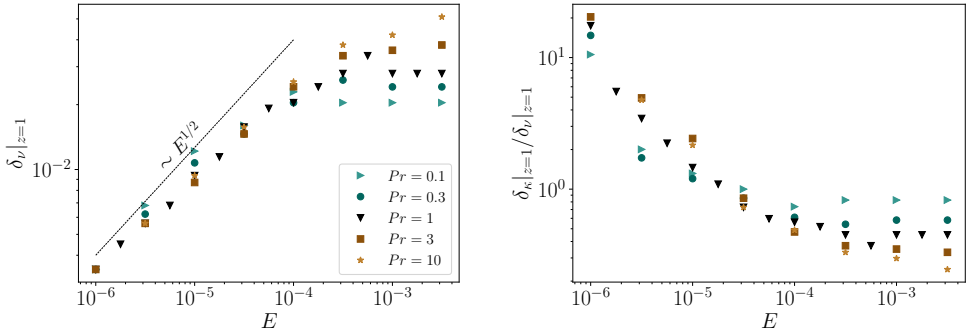


Figure 13: Left: top velocity boundary layer size as a function of E for $R = 10^{10}$. Right: ratio of thermal and velocity boundary layer size at the top plate as a function of rotation for $R = 10^{10}$ and several values of Pr .

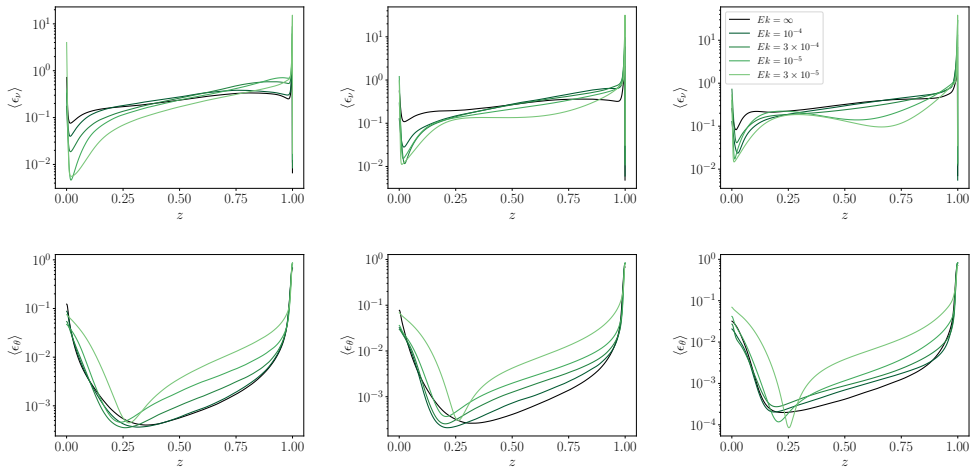


Figure 14: Kinetic $\langle \epsilon_\nu \rangle$ (top row) and thermal $\langle \epsilon_\theta \rangle$ (bottom row) profiles for $R = 10^{10}$ for several values of E and $Pr = 0.1$ (left column), $Pr = 1$ (middle) and $Pr = 10$ (right column).

4.4. Dissipation rates

To conclude the examination of rotation, we analyse the thermal $\overline{\langle \epsilon_\theta \rangle}$ and viscous $\overline{\langle \epsilon_\nu \rangle}$ dissipation rates (Figure 14). For $\overline{\langle \epsilon_\nu \rangle}$, the effect of rotation is qualitatively consistent across all Pr . Rotation suppresses dissipation in the bulk and bottom boundary layer while enhancing it near the top plate. This suppression is most visible at low Pr where the non-rotating flow was initially more turbulent close to the bottom plate. On the other hand, the thermal dissipation $\overline{\langle \epsilon_\theta \rangle}$ responds to rotation by increasing in the bulk and decreasing at the boundaries, regardless of Pr .

However, the impact on the total values of $\overline{\langle \epsilon_\theta \rangle}$ is more profound than on $\overline{\langle \epsilon_\nu \rangle}$. As shown in Figure 15, the bulk remains the dominant source of viscous dissipation across all E and Pr . In contrast, for thermal dissipation, the dominant contribution shifts from the top boundary layer to the bulk at high rotation rates ($E < 10^{-5}$). This transition in the dissipation budget suggests a fundamental change in the heat transport bottleneck as the system enters a

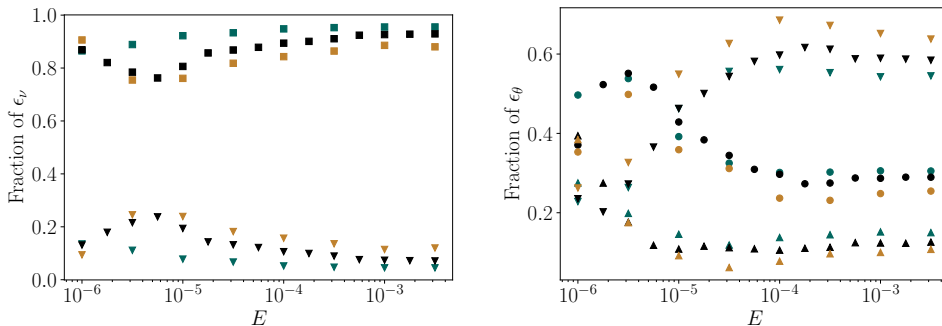


Figure 15: Relative contributions to the dissipation rates of the flow regions as a function of rotation for $R = 10^{10}$. Symbols: ∇ , top boundary layer; \circ , bulk; \triangle , bottom boundary layer; \square , bulk and bottom boundary layer combined.

rotationally constrained state. This is indicative of where we expect the geostrophic regime to arise, once R becomes large enough.

5. Conclusion and Outlook

In this study, we have numerically investigated the influence of the Prandtl number on internally heated convection (IHC) in both non-rotating and rotating regimes. By spanning two orders of magnitude in Pr ($0.1 \leq Pr \leq 10$) for rotating cases and three orders of magnitude for non-rotating cases, we have identified that while the global mean temperature $\langle T \rangle$ remains remarkably robust to changes in Pr , the underlying flow morphology and the distribution of local statistics are profoundly altered.

The most significant impact of Pr is observed in the lower, stably stratified portion of the fluid layer. In the non-rotating case, low Pr fluids experience a “symmetry recovery” where intense turbulent stirring from the bulk penetrates the stable layer, forcing it into a more active state. As Pr increases, the increased viscosity and decreased thermal diffusivity allow the stable stratification to dominate, eventually leading to a “dead zone” of nearly quiescent fluid at $Pr = 100$. This finding suggests that in geophysical contexts—where Pr can vary significantly—the “effective” depth of a convective layer might be dynamically determined by the Prandtl number, as high- Pr fluids effectively “mask” the lower portion of the domain from convective mixing.

The introduction of rotation introduces a competing mechanism of organisation. We find that rotation enhances vertical convective flux $\overline{\langle wT \rangle}$ across all Pr , but global heat transport efficiency (indicated by $\overline{\langle T \rangle}$) only improves for $Pr \geq 1$. This confirms that the Ekman pumping mechanism, which facilitates transport in rotating fluids, requires a sufficiently high Pr to overcome thermal diffusion, and is present in IHC.

Our results demonstrate that the analogy between IHC and Rayleigh-Bénard convection (RBC) is nuanced. While IHC shares many of the scaling behaviors of RBC at the top boundary, the stable stratification at the bottom create a unique sensitivity to the Prandtl number. Future work should explore the “infinite Pr ” limit more rigorously to see if the trends observed at $Pr = 100$ saturate, and whether the observed $R^{-0.2}$ scaling for temperature holds as the system approaches the fully geostrophic regime at even lower Ekman numbers. This would be particularly relevant for modeling the Earth’s mantle or the deep interiors of gas giants, where both internal heating and rotation are primary drivers of fluid motion.

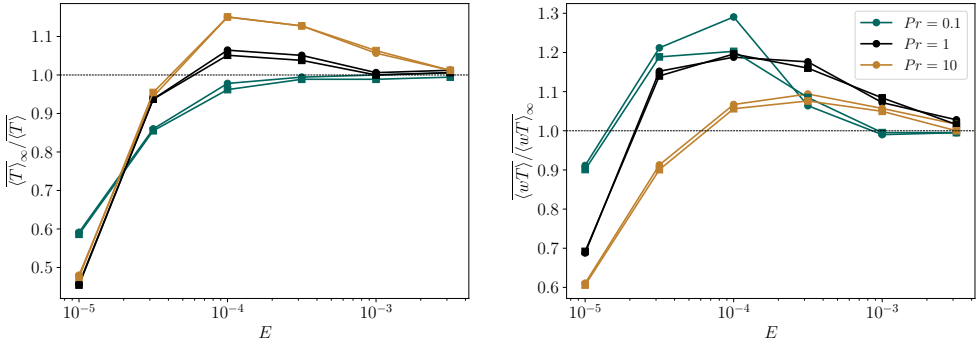


Figure 16: Changes in the global responses with rotation for $R = 10^9$ for $\Gamma = 1$ (round symbols) and $\Gamma = 2$ (square symbols).

Another direction of exploration is probing the stability of rotating IHC, particularly at low Prandtl numbers. For these control parameters, subcritical convection may be more important, significantly modifying the values of R and E for which convection appears.

Acknowledgments: ROM acknowledges support from the Emergia Program of the Junta de Andalucía (Spain). AA acknowledges funding from the ERC (agreement no. 833848-UEMHP) under the Horizon 2020 program and the SNSF (grant number 219247) under the MINT 2023 call. We also thank the Systems Unit of the Information Systems Area of the University of Cadiz for computer resources and technical support.

Declaration of Interests: The authors report no conflict of interest.

Appendix A. Dependence on domain size

In this section we briefly detail the studies on domain size independence. We first study the non-rotating case: we fix $R = 10^9$, and simulate $Pr = 0.1, 1$ and 10 for $\Gamma = 1$ and 2 . Grid resolution is kept the same as the number of points are doubled in the horizontal direction, i.e. $288^2 \times 144$ is used for $\Gamma = 1$ and $576^2 \times 144$ is used for $\Gamma = 1$.

The results obtained for the global quantities are presented in Table 1. We can observe how Re_w is the most sensitive quantity to Γ , presenting some dependence even for $Pr = 10$. On the other hand, $\overline{\langle wT \rangle}$ only shows Γ dependence for $Pr = 0.1$, and $\overline{\langle T \rangle}$ shows no significant Γ dependence across the Pr -range simulated.

Turning to the effect of rotation, in Figure 16 we show $\overline{\langle wT \rangle}$ and $\overline{\langle T \rangle}$ normalized by their respective non-rotating values (denoted by the subscript ∞) for both $\Gamma = 1$ and $\Gamma = 2$ for $R = 10^{10}$. We observe how the relative magnitude of increases in $\overline{\langle wT \rangle}$ are box-size dependent for $Pr = 0.1$, especially the peak at $E = 10^{-4}$, but not for the other two values of Pr . Even so, the increases persist. In addition, increases in $\overline{\langle T \rangle}$ are found to be Γ -independent regardless of Pr .

REFERENCES

- ABBATE, J. A. & AURNOU, J. M. 2023 Rotating convective turbulence in moderate to high prandtl number fluids. *Geophysical & Astrophysical Fluid Dynamics* **117** (6), 397–436.
- ARSLAN, A., FANTUZZI, G., CRASKE, J. & WYNN, A. 2021 Bounds on heat transport for convection driven by internal heating. *Journal of Fluid Mechanics* **919**, A15.
- ARSLAN, A. & ROJAS, R. E. 2025 New bounds for heat transport in internally heated convection at infinite prandtl number. *Journal of Mathematical Physics* **66** (2), 023101.

Pr	$ \Gamma $	$\overline{\langle wT \rangle}$	$\overline{\langle T \rangle}$	Re_w	$ \Gamma $	$\overline{\langle wT \rangle}$	$\overline{\langle T \rangle}$	Re_w
0.1	1	2.03×10^{-1}	1.78×10^{-2}	3.03×10^3	2	2.12×10^{-1}	1.77×10^{-2}	3.22×10^3
1	1	2.50×10^{-1}	1.65×10^{-2}	5.88×10^2	2	2.50×10^{-1}	1.64×10^{-2}	6.06×10^2
10	1	2.98×10^{-1}	1.68×10^{-2}	8.71×10^1	2	3.02×10^{-1}	1.68×10^{-2}	8.82×10^1

Table 1: Dependence on the horizontal periodicity length of the global responses.

- AURNOU, J. M., CALKINS, M. A., CHENG, J. S., JULIEN, K., KING, E. M., NIEVES, D., SODERLUND, K. M. & STELLMACH, S. 2015 Rotating convective turbulence in earth and planetary cores. *Physics of the Earth and Planetary Interiors* **246**, 52–71.
- CHANDRASEKHAR, S. 1953 The instability of a layer of fluid heated below and subject to coriolis forces. *Proceedings of the Royal Society of London. Series A. Mathematical and Physical Sciences* **217** (1130), 306–327.
- CHANDRASEKHAR, S. 1961 *Hydrodynamic and hydromagnetic stability*. Oxford University Pressn.
- ECKE, R. E. & SHISHKINA, O. 2023 Turbulent rotating rayleigh–bénard convection. *Annual review of fluid mechanics* **55**, 603–638.
- EMANUEL, K. A. 1994 *Atmospheric convection*. Oxford university press.
- GOLUSKIN, D. 2016 *Internally heated convection and Rayleigh–Bénard convection*. Springer Briefs in Applied Sciences and Technologies . Springer, Cham.
- GOLUSKIN, D. & VAN DER POEL, E. P. 2016 Penetrative internally heated convection in two and three dimensions. *Journal of fluid mechanics* **791**, R6.
- GOLUSKIN, D. & SPIEGEL, E. A. 2012 Convection driven by internal heating. *Physics Letters A* **377** (1-2), 83–92.
- GROOMS, I., JULIEN, K., WEISS, J. B. & KNOBLOCH, E. 2010 Model of convective taylor columns in rotating rayleigh–bénard convection. *Physical review letters* **104** (22), 224501.
- GROSSMANN, S. & LOHSE, D. 2000 Scaling in thermal convection: a unifying theory. *Journal of Fluid Mechanics* **407**, 27–56.
- KAZEMI, S., OSTILLA-MÓNICO, R. & GOLUSKIN, D. 2022 Transition between boundary-limited scaling and mixing-length scaling of turbulent transport in internally heated convection. *Physical Review Letters* **129** (2), 024501.
- KING, E. M. & AURNOU, J. M. 2013 Turbulent convection in liquid metal with and without rotation. *Proceedings of the National Academy of Sciences* **110** (17), 6688–6693.
- KING, E. M., STELLMACH, S., NOIR, J., HANSEN, U. & AURNOU, J. M. 2009 Boundary layer control of rotating convection systems. *Nature* **457** (7227), 301–304.
- KULACKI, FRANCIS ALFRED & GOLDSTEIN, RJ 1972 Thermal convection in a horizontal fluid layer with uniform volumetric energy sources. *Journal of Fluid Mechanics* **55** (2), 271–287.
- KUNNEN, R. P. J. 2021 The geostrophic regime of rapidly rotating turbulent convection. *Journal of Turbulence* **22** (4-5), 267–296.
- KUNNEN, R. P. J., OSTILLA-MÓNICO, R., VAN DER POEL, E. P., VERZICCO, R. & LOHSE, D. 2016 Transition to geostrophic convection: the role of the boundary conditions. *Journal of Fluid Mechanics* **799**, 413–432.
- LOHSE, D. & SHISHKINA, O. 2023 Ultimate turbulent thermal convection. *Physics Today* **1** **76**(11), 26–32.
- LOHSE, DETLEF & SHISHKINA, OLGA 2024 Ultimate rayleigh–bénard turbulence. *Reviews of modern physics* **96** (3), 035001.
- MAFFEI, S., KROUSS, M. J., JULIEN, K. & CALKINS, M. A. 2021 On the inverse cascade and flow speed scaling behaviour in rapidly rotating rayleigh–bénard convection. *Journal of Fluid Mechanics* **913**, A18.
- MARSHALL, J. & SCHOTT, F. 1999 Open-ocean convection: Observations, theory, and models. *Reviews of geophysics* **37** (1), 1–64.

- OSTILLA-MÓNICO, R. & ARSLAN, A. 2025 Rotationally affected internally heated convection. *Journal of fluid mechanics* **1018**, A31.
- ROBERTS, P. H. 1967 Convection in horizontal layers with internal heat generation. Theory. *Journal of Fluid Mechanics* **30** (1), 33–49.
- ROBERTS, P. H. & KING, E. M. 2013 On the genesis of the earth’s magnetism. *Reports on Progress in Physics* **76** (9), 096801.
- STEVENS, R. J. A. M., CLERCX, H. J. H. & LOHSE, D. 2010a Optimal prandtl number for heat transfer in rotating rayleigh–bénard convection. *New Journal of Physics* **12** (7), 075005.
- STEVENS, R. J. A. M., CLERCX, H. J. H. & LOHSE, D. 2013 Heat transport and flow structure in rotating rayleigh–bénard convection. *European Journal of Mechanics-B/Fluids* **40**, 41–49.
- STEVENS, R. J. A. M., VERZICCO, R. & LOHSE, D. 2010b Radial boundary layer structure and nusselt number in rayleigh–bénard convection. *Journal of Fluid Mechanics* **643**, 495–507.
- THIRLBY, R. 1970 Convection in an internally heated layer. *Journal of Fluid Mechanics* **44** (4), 673–693.
- TRITTON, D. J. & ZARRAGA, M. N. 1967 Convection in horizontal layers with internal heat generation. experiments. *Journal of Fluid Mechanics* **30** (1), 21–31.
- VAN DER POEL, E. P., OSTILLA-MÓNICO, R., DONNERS, J. & VERZICCO, R. 2015 A pencil distributed finite difference code for strongly turbulent wall-bounded flows. *Computers & Fluids* **116**, 10–16.
- VERONIS, G. 1959 Cellular convection with finite amplitude in a rotating fluid. *Journal of Fluid Mechanics* **5** (3), 401–435.
- VOROBIEFF, P. & ECKE, R. E. 2002 Turbulent rotating convection: an experimental study. *Journal of Fluid Mechanics* **458**, 191–218.
- WANG, Q., LOHSE, D. & SHISHKINA, O. 2020 Scaling in internally heated convection: a unifying theory. *Geophysical Research Letters* **47**, e2020GL091198.
- ZHONG, J., STEVENS, R. J. A. M., CLERCX, H. J. H., VERZICCO, R., LOHSE, D. & AHLERS, G. 2009 Prandtl-, rayleigh-, and rossby-number dependence of heat transport in turbulent rotating rayleigh–bénard convection. *Phys. Rev. Lett.* **102**, 044502.